Surface states and series resistance effects in Au/(HgS-PVA)/n-Si capacitors

Ömer Sevgili[1],[*] , İlke Taşçıoğlu[2], Sana Boughdachi[3], Seçkin Altındal Yerişkin[4], and Yashar Azizian-Kalandaragh[5],[6]

[1] *Faculty of Engineering and Natural Sciences, Kütahya Health Sciences University, 43020 Kütahya, Turkey*

[2] *Department of Electrical and Electronics Engineering, Faculty of Engineering, Istanbul Topkapi University, 34662 Istanbul, Turkey*

[3] *Department of Physics, University of Amsterdam, Science Park 904, 1090, GL, Amsterdam, The Netherlands*

[4] *Department of Chemistry and Chemical Processing Technologies, Vocational Highschool of Technical Sciences, Gazi University, 06560 Ankara, Turkey*

[5] *Department of Photonics, Faculty of Applied Sciences, Gazi University, 06500 Ankara, Turkey*

[6] *Department of Physics, University of Mohaghegh Ardabili, P.O. Box.179, Ardabil, Iran*

ABSTRACT

HgS nanomaterials were synthesized using an ultrasound-assisted method, and their optical and morphological properties were analyzed through UV–Vis spectroscopy and scanning electron microscopy (SEM). The capacitance–voltage (C–V) and conductance–voltage (G/ω–V) measurements of the Au/(HgS-PVA)/n-Si (MPS) capacitor were conducted across a frequency range of 1 kHz–5 MHz. The experimental data were used to investigate the effects of surface states (N_{ss}) and series resistance (R_s). Both C and G/ω increased at lower frequencies, as the surface states could follow the AC signal, contributing to the overall response. The density of N_{ss} was derived using the high-low frequency (HF) capacitance method and parallel conductance technique, while Nicollian–Brews' method was employed to extract the R_s. This study reveals that the conductance method yields higher values than the HF C–V method, attributed to its sensitivity to fast interface states and distributed trap time constants. The observed frequency-dependent losses in G_p/ω measurements confirm the presence of a continuous trap distribution near the HgS-PVA/n-Si surface, significantly influencing device reliability. The average N_{ss} was calculated to be ~ 10^{12} eV^{-1} cm^{-2}, indicating a well-controlled interface. The obtained N_{ss} and R_s values suggest that the HgS-PVA nanocomposite is a promising alternative to conventional insulating layers (e.g., SiO$_2$ or SnO$_2$) in electronic devices, thanks to its favorable electrical properties.

 Springer

1 Introduction

Nanocrystalline materials demonstrate significant potential for investigation across various scientific disciplines, including chemistry, physics, and engineering. In particular, semiconductor nanostructures have been the subject of extensive investigation over several decades, given that their distinctive properties diverge from those observed in their bulk counterparts. These properties are frequently attributed to the high surface-to-volume ratio resulting from quantum confinement, which arises from the nanoscale dimensions of the materials in question [1–3]. One of the most significant consequences of reducing the dimensions of materials to the nanometer scale is the emergence of quantization effects, which arise from the confinement of electron movement. This results in the formation of discrete energy levels, which depend on the dimensions of the structure in question [4, 5]. Mercury Sulfide (HgS) with a small band gap (1.9–2.6 eV) is a critical semiconductor compound in the II-VI group [6–9]. It offers a wide potential for use in various disciplines and has an important place in technological applications. The HgS is known to exist in at least two distinct crystalline modifications. Cinnabar (α-HgS) is red, whereas meta-cinnabar (β-HgS) is black [6–8]. These include use as electrostatic image materials, catalysts, image sensors, infrared detectors, ultrasonic transducers, acoustic-optical materials, light-emitting diodes, Schottky barrier diodes (SBDs), and more [9–13]. A plethora of methodologies have been devised for the synthesis of mercuric sulfide nanostructures, including microemulsion templates, hydrothermal, sol–gel, microwave-assisted, solid-state reaction at elevated temperatures, biosynthesis, Langmuir–Blodgett (LB), single-source precursor, and ultrasound-assisted (Sono-chemical) techniques [7, 14–17]. Among these methods, ultrasound-assisted process stands out as the most promising approach for nanomaterial synthesis due to its ease of processing and precise particle size control.

Metal–semiconductor (MS) structures comprising a thick insulator/oxide–semiconductor, polymer, and ferroelectric are known to be capable of storing increasingly large electric charges or energy [18–24]. Several factors can lead to discrepancies between the observed behavior of a capacitor and the ideal behavior predicted by theory. These include the presence of surface states (N_{ss}) with different relaxation times located at the interfacial layer/semiconductor surface

and band gap of the semiconductor, series resistance (R_s) of the device, surface preparation, and inhomogeneity of the barrier between the metal and the semiconductor [25–30]. It was hypothesized that an interfacial layer with a high dielectric constant would exhibit excellent surface passivation properties on a crystalline semiconductor. In other words, attempts have been made to improve or modify the electrical and optical properties of MS-based devices by employing metal or graphene-doped polymer composite interfacial layers. These attempts are motivated by the technical importance of these flexible materials, which are low-cost to produce, perform well, have a low molecular weight, can be produced on a large scale, and can be processed easily in comparison to traditional SiO_2 or SnO_2 interlayer [21–23, 31–33].

Some researchers have recently done the studies on the various polymer materials [34–41]. This work analyzes the structural and optical properties of HgS nanomaterials synthesized by ultrasonically assisted method, forming a Polyvinyl Alcohol (PVA)-based interlayer with these materials and fabricating a metal-polymer-semiconductor (MPS) type capacitor in Au/(HgS-PVA)/n-Si configuration. Due to the homogeneous and controlled size distribution of HgS nanomaterials, the series resistance values of the capacitors can be significantly reduced, making the devices suitable for high-energy storage applications. There are very limited studies on HgS/PVA nanocomposites and devices based on this material in the literature. In our previous work, a detailed study of the dielectric behavior and polarization processes was carried out for the same diode. One of the most critical factors affecting the performance of SBD is the properties of the N_{ss} at the interfacial layer/semiconductor surface. In addition, calculating the time constant helps to understand the dynamic interactions of interfacial states with charge carriers. This information can be used to optimize carrier recombination and relaxation processes. The parallel conductance method provides a powerful tool for understanding and optimizing the impact of these states on device characteristics. The N_{ss} and their τ profiles were obtained from the conductance method in the frequency range of 1 kHz–5 MHz at RT. Furthermore, the results obtained from the C_{HF}–C_{LF} method for the fabricated capacitor are compared. Furthermore, an in-depth investigation has been conducted into the sources of N_{ss} and R_s. In summary, the optical and morphological properties of HgS nanostructures obtained using the

ultrasound-assisted approach were investigated in this study. In addition, the effects of the (HgS-PVA) composite structure formed by HgS-PVA nanostructures with PVA polymer on the electrical behavior of the Au/(HGS-PVA)/n-Si capacitor structure were evaluated by impedance spectroscopy. In this context, the N_{ss} and R_s profiles were investigated under the influence of these nanostructures. Therefore, impedance spectroscopy measurements were performed over a wide frequency range in the frequency range of 1 kHz– MHz at room temperature (RT). Moreover, the potential of this interface layer in electronic applications was tried to be revealed.

2 Experimental procedures

2.1 Synthesis of HgS-PVA nanocomposites

The materials employed were mercury(II) nitrate ($Hg(NO_3)_2$), sodium sulfate (Na_2SO_4), sodium hydroxide (NaOH), and ethanol (absolute), which were supplied by Merck and used directly without purification. The following standard procedure conducted the preparation of HgS nanostructures: To create a 0.2 M solution, 1.37 g $Hg(NO_3)_2$ and 0.96 g $Na_2S_*9\ H_2O$ were combined in 20 mL of distilled water. Using an ultrasound processor, this solution was subjected to high-intensity ultrasound irradiation under ambient air for 15 min. Upon completion of the reaction, the

precipitates were subjected to centrifugation, followed by washing with distilled water and ethanol five times. They were then dried in air at RT.

The preparation of the HgS-PVA film commenced with creating an aqueous PVA solution (5%) through the gradual dissolution of PVA in deionized water. This was accomplished by heating at 85 °C for two hours while swirling magnetically. The transparent aqueous PVA solution was allowed to cool at RT to obtain gel formation. Furthermore, a HgS-PVA composite material was created in a standard experiment by mixing 10 ml of 5% aqueous PVA solution with 0.2 g of the produced HgS powder. It was then subjected to ultrasonic irradiation at room temperature (RT) for 5 min. Therefore, viscous and well-dispersed HgS-PVA composite gels were produced.

2.2 Morphological analysis

Scanning Electron Microscope (SEM) was used to observe the surface morphology of the Sono-chemically prepared HgS nanostructures. Figure 1 demonstrates that the particles are spherical and exhibit regular morphology with a nanoscale size distribution.

2.3 UV–Vis analyses

Ultraviolet–Visible (UV–Vis) spectroscopy was used to investigate the prepared sample's optical properties. Figure 2 displays the absorption spectra captured in
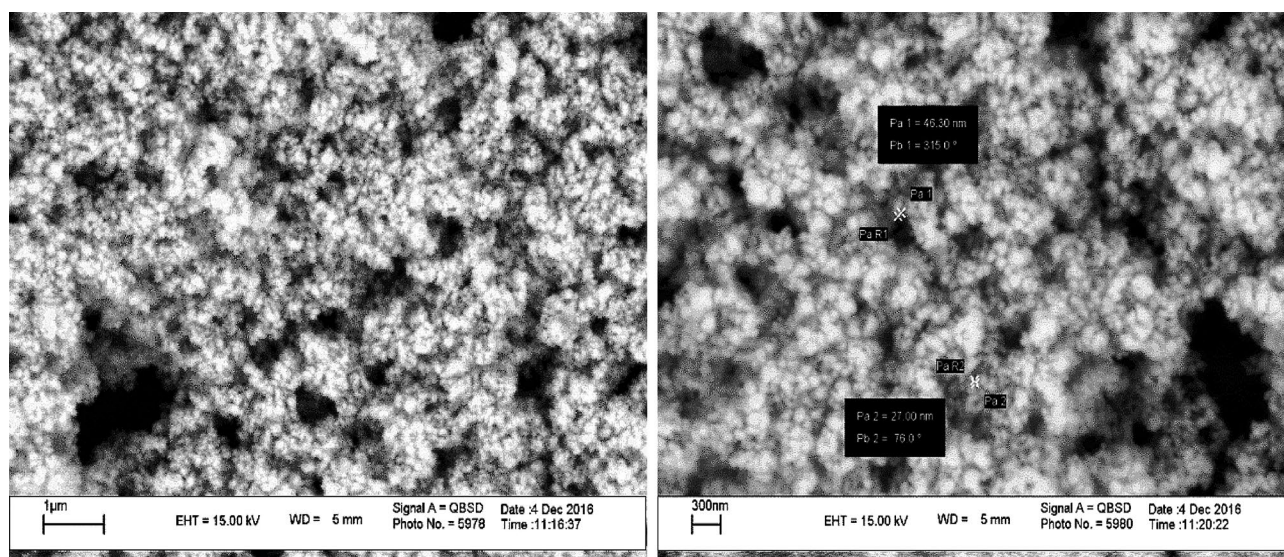

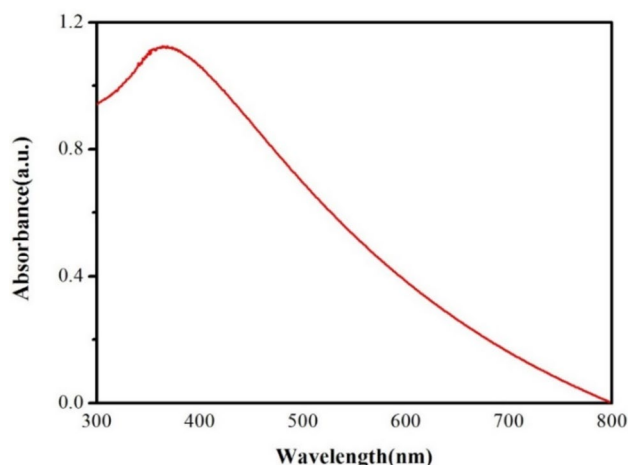**Fig. 1** SEM pictures of the HgS nanostructures with various magnifications

Fig. 2 Absorption spectra of the HgS nanostructures

Fig. 3 Schematic diagram of Au/HgS-PVA/n-Si (MPS) capacitor

the wavelength range of 300–800 nm, showing a peak at approximately 375 nm.

2.4 Manufacture of Au/HgS-PVA/n-Si (MPS) capacitors

Details of the device fabrication can be found in Ref [42]. In summary, the semiconductor was first cleaned in methanol and then rinsed in deionized water in an ultrasonic bath for 5 min. Then, it was soaked in a solution of H_2O, NH_4OH, and H_2O_2 (65:13:13 v/v) and washed again in deionized water. Finally, it was soaked in a solution of H_2O:HF (24:1 v/v) and washed again in deionized water. In the thermal evaporation system, 99.999% pure gold (Au) metal was evaporated onto the back surface of the semiconductor to form an ohmic contact. The semiconductor was then annealed at 500 °C to obtain low resistivity. HgS-PVA nanocomposites were coated onto the front surface of the semiconductor using the electrospinning method. The device fabrication was completed by obtaining Au rectifier contacts using a shadow mask in thermal evaporation. A schematic diagram of the capacitor is provided in Fig. 3.

3 Results and discussion

Frequency-dependent capacitance and conductance characteristics are important tools for understanding the surface states' interaction rate with energy levels in SBDs and the electrical stability of the
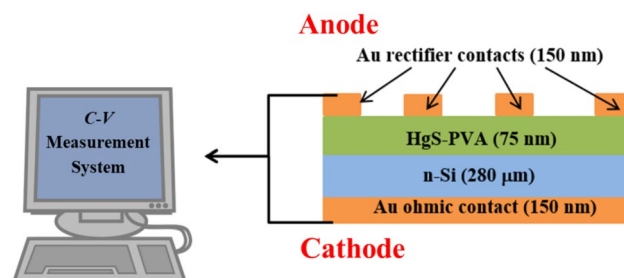
device. Figures 4 and 5 illustrate the MPS capacitor's admittance (C–V and G/ω–V) characteristics within 1 kHz–5 MHz, respectively. A pronounced frequency dependence of C and G/ω values in the depletion and accumulation zones was observed, primarily caused by N_{ss}, surface polarization, R_s, and the interfacial layer. Notably, N_{ss} and surface polarization perform well at low frequencies in the inversion and depletion zones. However, R_s is only effective in the accumulation zone, and especially at high frequencies. As illustrated in Fig. 5, the G/ω-V plots exhibit a peak in the depletion zone at low frequencies, ascribed to the peculiar density distribution of the N_{ss} and polarization-induced surface dipole moment. The magnitude of the peak diminishes with rising frequencies, shifting toward the accumulation zone. This is because the charges in the states respond to a small AC signal only if the band bending is sufficient to shift the trap level across the Fermi energy (E_F).

The R_s significantly impacts the admittance characteristics in the accumulation zone. Its real value is determined by the C and G/ω values when the capacitor is in the strong accumulation zone at each frequency, as shown in Fig. 6. Nicollian and Brews derived the following relation to obtain the resistance (R_i) values for each frequency as a function of voltage [19].

$$R_s = \frac{G_{ma}}{G_{ma}^2 + (\omega C_{ma})^2} \tag{1}$$

In Eq. (1), C_{ma} and G_{ma} represent the measured capacitance and conductance, respectively, at the strong accumulation zone [43–45]. The voltage-dependent profile of R_s was obtained from Eq. (1) for each frequency and is represented in Fig. 6. As illustrated in Fig. 6, the value of R_s exhibits a decline with an increase in frequency for each bias voltage.

Fig. 4 The *C–V* plot of the Au/HgS-PVA/n-Si (MPS) capacitor for various frequencies at RT
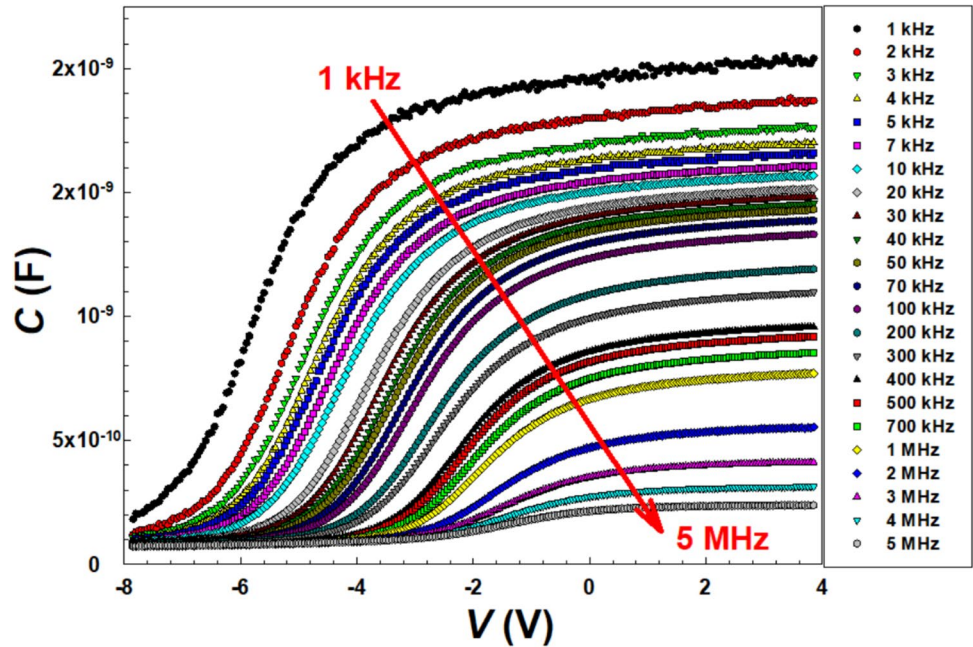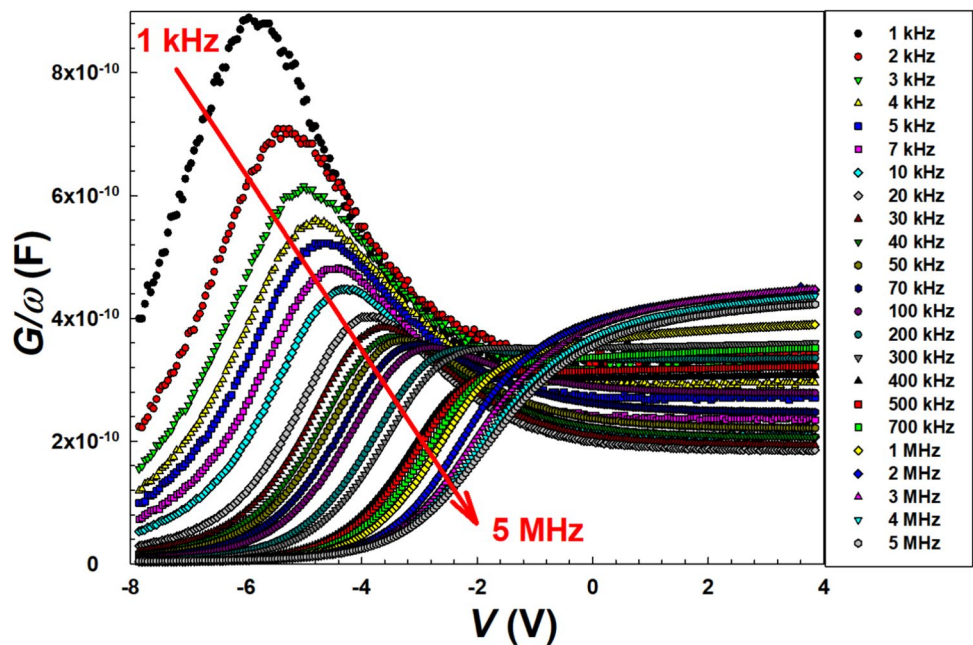

Fig. 5 The *G/ω-V* plots of the Au/HgS-PVA/n-Si (MPS) capacitor for various frequencies at RT

However, its actual value aligns with that of the strong accumulation zone at sufficiently high frequencies ($f \geq 1$ MHz). It is evident that the R_s value of the Au/HgS-PVA/n-Si (MPS) capacitor is markedly low, rendering it highly suitable for incorporation into an electronic device. In general, R_s can arise from various sources, but the most significant of these are: (1) the contact formed by the probe wire with the rectifier contact; (2) the back contact with the back side of the semiconductor; (3) impurities between the back contact and the ground; and (4) the resistance of bulk semiconductor (5) interface quality (6) surface roughness etc. [18, 46, 47]. The impact of R_s can be disregarded at low frequencies; however, at high frequencies, it can be mitigated by correcting the admittance measurements before extracting the desired information.
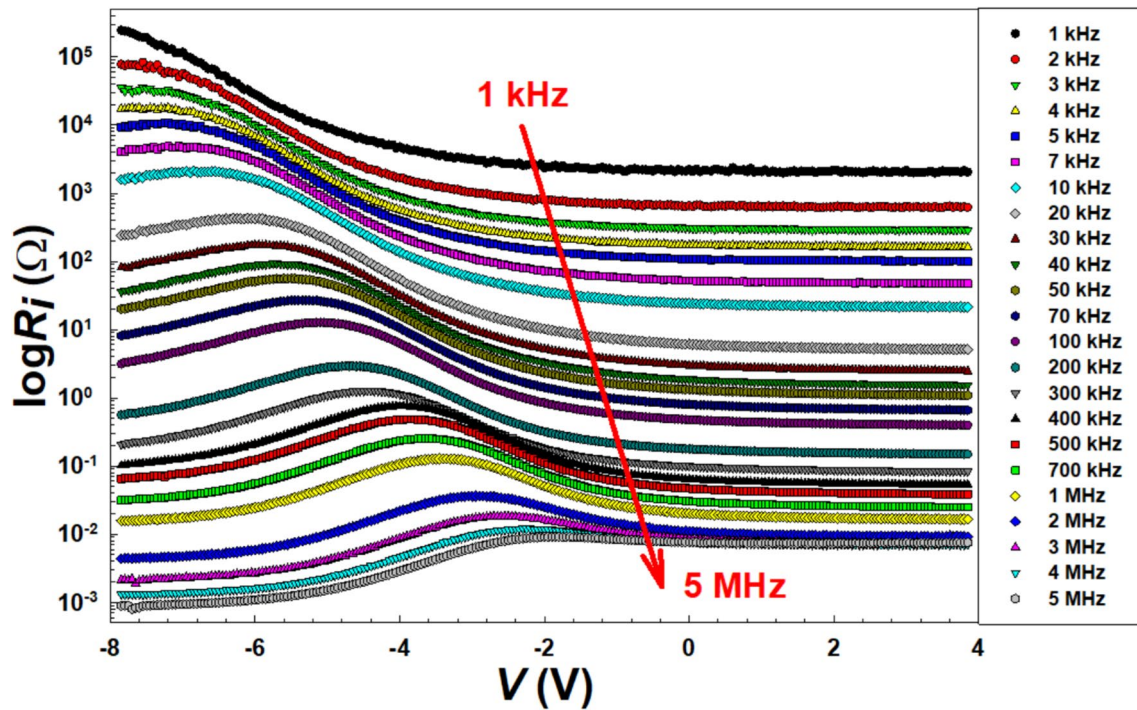
Fig. 6 The R_i-V plot of the Au/HgS-PVA/n-Si (MPS) capacitor for various frequencies at RT

Fig. 7 Equivalent circuits for conductance technique; **a** a conventional MOS capacitor, **b** simplified circuit of **a**, **c** circuit of the measured circuit
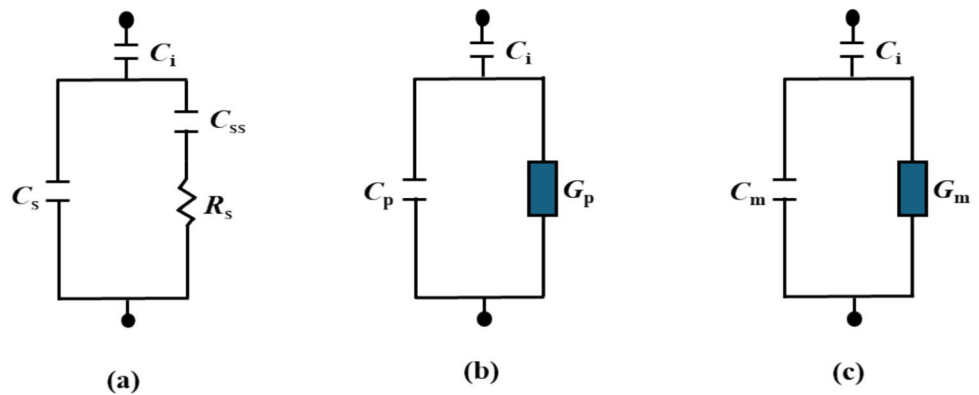

Figure 7 illustrates the equivalent circuits of a MOS-type capacitor employed in the conductance method. Figure 7a illustrates the capacitive components of the structure. Here, C_{ss}, C_i, C_s, and R_s represent the capacitance of surface states, the oxide/polymer interlayer capacitance, the semiconductor capacitance, and the resistance indicating the loss processes when N_{ss} capture and emit carriers, respectively. However, for the parallel conductance (G_p), it is possible to replace the circuit shown in Fig. 7a with the circuit shown in Fig. 7b. In this case, the parallel capacitance (C_p) and G_p are given by:

$$C_p = C_s + \frac{C_{ss}}{1 + (\omega\tau)^2} \tag{2}$$

$$\frac{G_p}{\omega} = \frac{q\omega\tau N_{ss}}{1 + (\omega\tau)^2} \tag{3}$$

Here, $C_{ss} = q^2 N_{ss}$, $\tau = R_s N_{ss}$ (time constant of the N_{ss}), and $\omega = 2\pi f$ (angular frequency). The N_{ss} is not confined to a single energy level in the energy band but, instead, exhibits a distribution within the energy band of the semiconductor and at the semiconductor/polymer interface. The capture and emission

processes are mainly facilitated by traps situated within a small energy range of kT/q above and the Fermi level. This causes a variation in time constants and influences the normalized conductance given as [19, 48]:

$$\frac{G_P}{\omega} = \frac{qN_{ss}}{2\omega\tau}\ln\left[1 + (\omega\tau)^2\right] \tag{4}$$

In admittance measurements, impedance meters will presume the device is a parallel mix of C_m and G_m. By transforming the circuit depicted in Fig. 7b into the circuit illustrated in Fig. 7c, it is possible to express G_p/ω;

$$\frac{G_P}{\omega} = \frac{\omega G_m C_i^2}{G_m^2 + \omega^2\left(C_i - C_m\right)^2} \tag{5}$$

In order to analyze N_{ss}, C_m and G_m/ω were plotted as a function of frequency for a range of applied bias voltages in the depletion zone, presented in Fig. 8a and b, respectively.

As illustrated in Fig. 8a and b, C_m and G_m/ω exhibit a pronounced dependence on frequency, particularly in the depletion zone due to the presence of N_{ss}. However, they become almost independent of frequency in this region. The peak behavior observed in the G_m/ω-log$f$ plot has been attributed to the specific density distribution of N_{ss} at HgS-PVA/Si interface, as well as interfacial polarization [49–51].

Accordingly, the G_p/ω-log$f$ plot for the Au/HgS-PVA/n-Si (MPS) capacitor was constructed to ascertain the values of N_{ss}, presented in Fig. 9. The distributions of G_p/ω maxima indicate how much the band bends in response to the applied gate bias voltage. The band bending seems more substantial when $(G_p/\omega)_{max}$ decreases and shifts toward the inversion zone. The maximum value of G_p/ω is observed at $\omega = 1/\tau$. Consequently, the values of N_{ss} and τ for the Au/HgS-PVA/n-Si (MPS) capacitor were obtained from the peak value of $(G_p/\omega)_{max}$ and its peak frequency. As illustrated in Fig. 10, while the value of τ decreases with increasing frequency almost as exponentially, N_{ss} decreases. The G_p/ω vs log$f$ characteristic arises due to a broad spectrum of interface trap states. At a fixed bias voltage, the position of the Fermi level dictates how these trap states are filled, influencing the charge density at the HgS-PVA/n-Si surface and setting the relaxation time of the corresponding N_{ss}. Maximum energy dissipation (peak

loss) happens when the AC signal's frequency aligns with this characteristic time. However, if the frequency differs slightly, the losses diminish because the traps either cannot follow the signal or respond out of phase, resulting in a distinct loss peak across the frequency spectrum [52, 53]. The mean value of N_{ss} for the Au/HgS-PVA/n-Si (MPS) capacitor was approximately 10^{12} eV^{-1} cm^{-2}, which is more appropriate for these types of devices. The low value of N_{ss} indicates that the (HgS-PVA) interfacial polymer layer can be an alternative to conventional oxide layers due to its ability to passivate N_{ss}.

An alternative method for extracting the N_{ss} is to measure the C_m at a fixed low and high frequency. In other words, the N_{ss} can be determined by measuring the C_m at a fixed high frequency ($f \geq 1$ MHz) and a fixed low frequency ($f \leq 1$ kHz), which is known as the high-low frequency capacitance method (C_{HF}–C_{LF}) using Eq. 6 [23]. At elevated frequencies, N_{ss} is unable to track an external AC signal across the entire measurement range; thus, it does not contribute to excess capacitance. However, when the frequency decreases sufficiently, all N_{ss} can respond to the signal. Consequently, the voltage-dependent profile of N_{ss} was also retrieved from the difference of the high–low (1 MHz–1 kHz) C–V plots for the entire measurement range, as illustrated in Fig. 11. It is evident that this method is more straightforward and time-efficient than the conductance method, while yielding comparable results.

$$N_{ss} = \frac{1}{qA}\left[\left(\frac{1}{C_{LF}} - \frac{1}{C_i}\right)^{-1} - \left(\frac{1}{C_{HF}} - \frac{1}{C_i}\right)^{-1}\right] \tag{6}$$

where C_{LF} stands for low-frequency capacitance (1 kHz) and C_{HF} for high-frequency capacitance (1 MHz). Similar results on the voltage-dependent profiles of R_s and N_{ss} were also reported by different researchers in recent years [52–62].

4 Conclusion

In this study, the HgS nanomaterials were prepared by the ultrasound-assisted technique. SEM images confirmed that the particles are spherical and exhibit regular morphology with a nanoscale size distribution. UV–Vis measurements confirmed the absorption spectra captured in the wavelength range of 300–800 nm, showing a peak at approximately 375

Fig. 8 a The C_m versus log$f$ plot and **b** the G_m/ω versus log$f$ plot of the Au/HgS-PVA/n-Si (MPS) capacitor for various voltages at RT
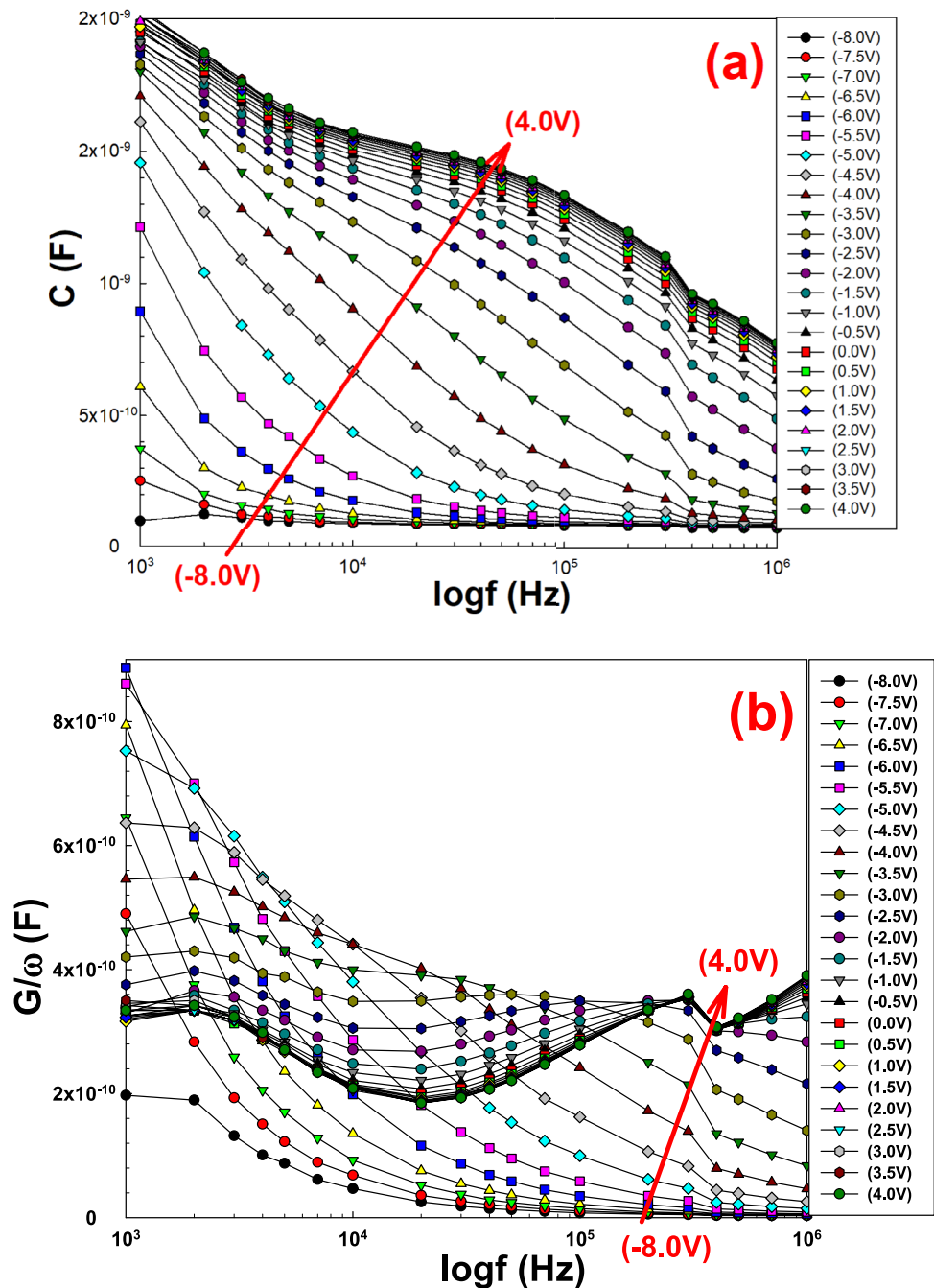
nm. HgS-PVA material was introduced between the Au and n-Si layers using the electrospinning method. The frequency-dependent electrical characteristics of the produced Al/(HgS-PVA)/n-Si structures were also characterized using C–V and G/ω-V measurements in the frequency range of 1 kHz–5 MHz at RT. The experimental results demonstrate that C and G are markedly influenced by frequency and voltage, particularly in the depletion and accumulation zones where N_{ss} and R_s are effective. Parallel conductivity (G_p/ω)-log$f$ graphs revealed distinct peaks at varying voltage levels. These peaks rose with increasing voltage and shifted toward the accumulation area. The R_s profile was obtained using the Nicollian–Brews

Fig. 9 The G_p/ω-log (f) plot for the Au/HgS-PVA/n-Si (MPS) capacitor at RT
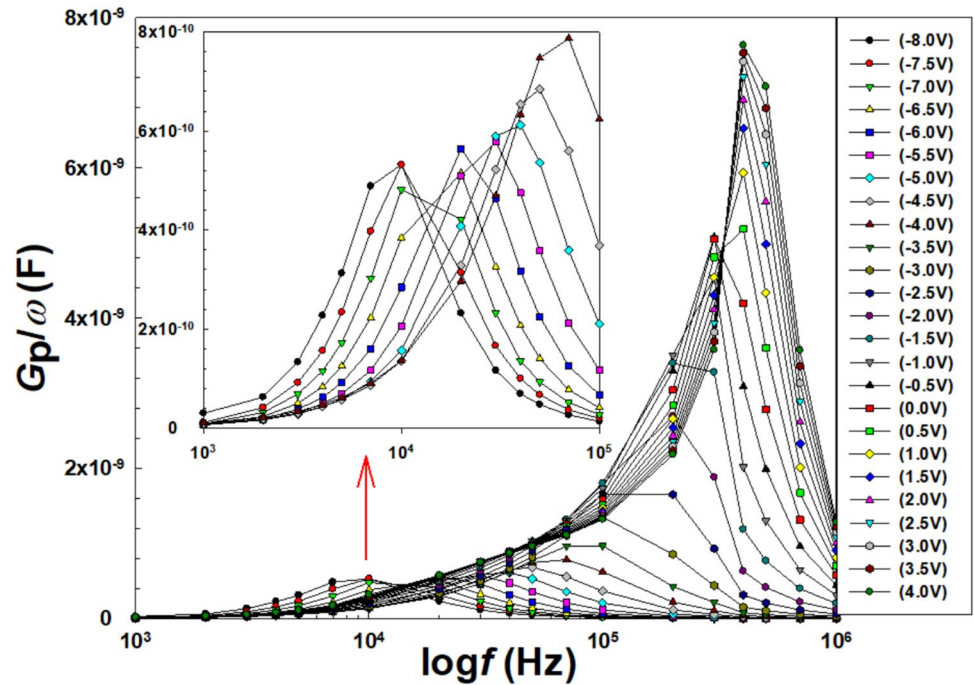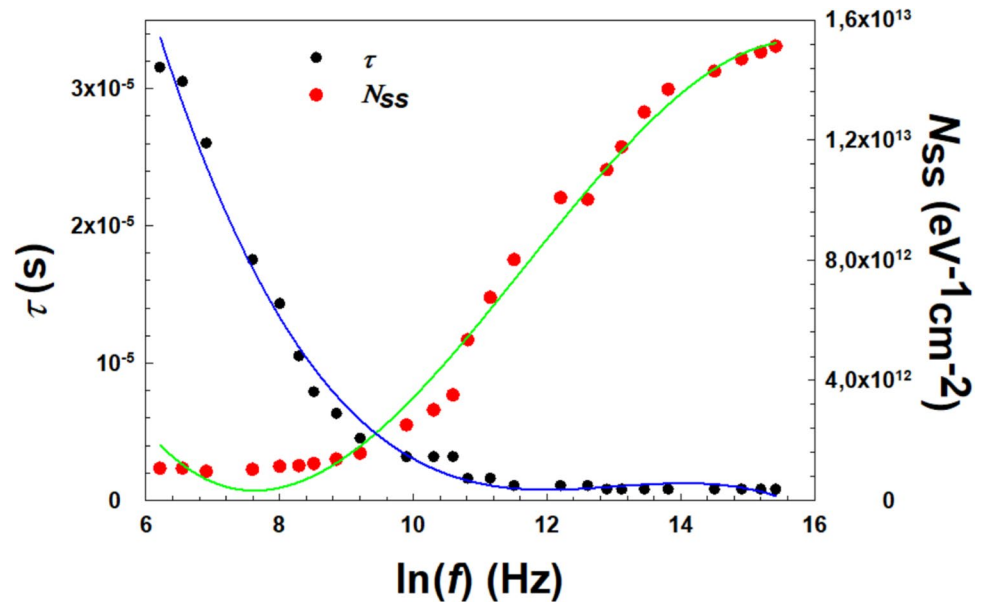

Fig. 10 N_{ss} and τ versus ln(f) plot for the Au/HgS-PVA/n-Si (MPS) capacitor at RT

method, while the N_{ss} profile was extracted using high-low frequency capacitance and the parallel conductance methods. The high-low frequency capacitance approach yielded similar N_{ss} values, with an average of approximately 10^{12} eV^{-1} cm^{-2}. The R_s of the capacitor was observed to decrease with increasing frequency. These findings suggest that the utilization of HgS-PVA interlayer may offer a viable alternative to the conventional interlayer, with the potential to enhance the quality and performance of the capacitor. In other words, this it can be used in the field of embedded devices for high charge/energy storage capacitors.

Fig. 11 The N_{ss}-V plot of the Au/HgS-PVA/n-Si (MPS) capacitor obtained from the C_{LF}–C_{HF} frequency capacitance method at RT
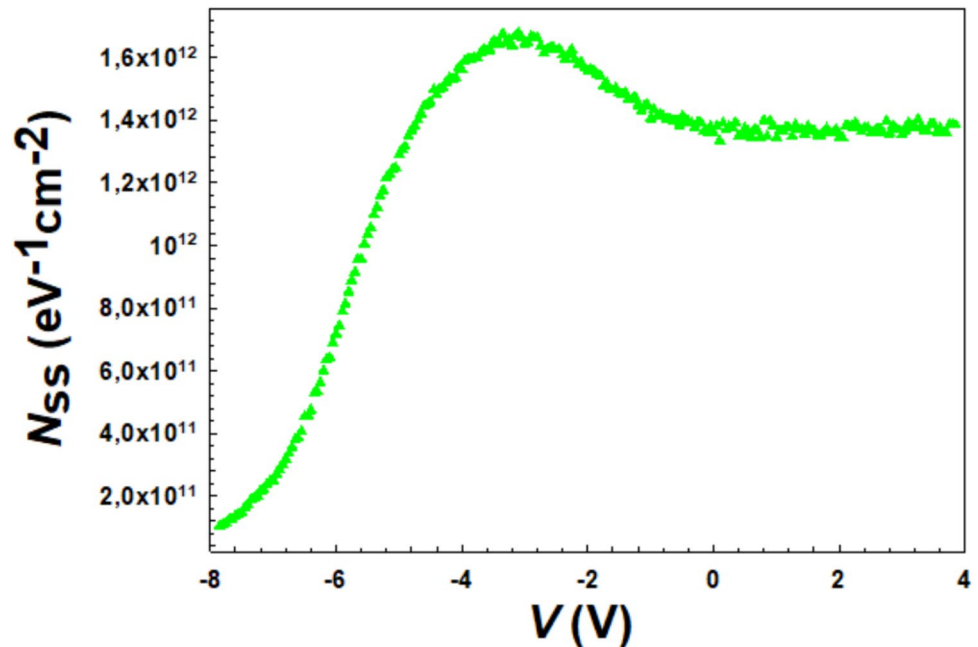
Author contributions

ÖS contributed in writing original draft, formal analysis, methodology, data curation and conceptualization. İT contributed in writing original draft, editing, formal analysis, data curation, conceptualization and supervision. SB contributed in writing original draft, formal analysis, methodology, data curation and conceptualization. SAY contributed in writing original draft, formal analysis, data curation and conceptualization. YA contributed in writing original draft, editing, methodology, data curation, data formal analysis, validation, visualization, conceptualization and supervision.

Funding

Data availability

All the data generated or analyzed during this study are included in this published article.

Declaration

Conflict of interest The authors declare that they have no conflict of interest.

References

1. R.S. Devan, R.A. Patil, J.-H. Lin, Y.-R. Ma, Adv. Funct. Mater. **22**, 3326 (2012)

2. S. Soleimani, A. Salabat, R.F. Tabor, J. Colloid Interface Sci. **426**, 287 (2014)

3. B. Ajitha, Y. Ashok Kumar Reddy, P. Sreedhara Reddy, Powder Technol. **269**, 110 (2015)

4. M. Kooti, L. Matturi, Int. Nano Lett **1**, 38 (2011)

5. G. Anandha Babu, G. Ravi, Y. Hayakawa, M. Kumaresavanji, J. Magn. Magn. Mater. **375**, 184 (2015)

6. K.M. Freny Joy, N. Victor Jaya, J. Phys. Sci. Appl. **6**, 59 (2016)

7. J. Zhu, S. Liu, O. Palchik, Y. Koltypin, A. Gedanken, J. Solid State Chem. **153**, 342 (2000)

8. C. Miguel, J.V. Pinto, M. Clarke, M.J. Melo, Dye. Pigment. **102**, 210 (2014)

9. H. Safardoust-Hojaghan, M. Shakourı-Aranı, M. Salavatı-Nıasarı, Trans. Nonferrous Met. Soc. China **26**, 759 (2016)

10. K. Higginson, M. Kuno, J. Bonevich, S. Qadri, M. Yousuf, H. Mattoussi, J. Phys. Chem. B **106**, 9982 (2002)

11. A. Sobhani, M. Salavati-Niasari, M. Sobhani, Mater. Sci. Semicond. Process. **16**, 410 (2013)

12. J. Sapriel, Appl. Phys. Lett. **19**, 533 (1971)

13. A. Hagfeldt, M. Graetzel, Chem. Rev. **95**, 49 (1995)

14. I. Mukherjee, S. Senapati, D. Mitra, A.K. Rakshit, A.R. Das, S.P. Moulik, Colloids Surfaces A Physicochem. Eng. Asp. **360**, 142 (2010)

15. X. Chen, X. Wang, Z. Wang, X. Yang, Y. Qian, Cryst. Growth Des. **5**, 347 (2005)

16. C. Zylberajch, A. Ruaudel-Teixier, A. Barraud, Synth. Met. **27**, 609 (1988)

17. J.Z. Mbese, P.A. Ajibade, Polymers (Basel). **6**, 2332 (2014)

18. S.M. Sze, *Physics of Semiconductor Devices*, 2nd edn. (Willey, New York, 1981)

19. E.H. Nicollian, J.R. Brews, *Metal Oxide Semiconductor (MOS) Physics and Technology* (John Wiley & Sons, New York, 1982)

20. Y. Şafak-Asar, T. Asar, Ş Altındal, S. Özçelik, J. Alloys Compd. **628**, 442 (2015)

21. M. Siva Pratap Reddy, J.-H. Lee, J.-S. Jang, Synth. Met. **185–186**, 167 (2013)

22. V. Rajagopal Reddy, V. Manjunath, V. Janardhanam, Y.-H. Kil, C.-J. Choi, J. Electron. Mater. **43**, 3499 (2014)

23. S.A. Yeriskin, H.I. Unal, B. Sari, J. Appl. Polym. Sci. **120**, 390 (2011)

24. İ Taşçıoğlu, M. Soylu, Ş Altındal, A.A. Al-Ghamdi, F. Yakuphanoglu, J. Alloys Compd. **541**, 462 (2012)

25. S. Altindal, Y.Ş Asar, A. Kaya, Z. Sönmez, J. Optoelectron. Adv. Mater. **14**, 998 (2012)

26. J. Ho, T.R. Jow, S. Boggs, I.E.E.E. Electr, Insul. Mag. **26**, 20 (2010)

27. A. Heime, H. Pagnia, Appl. Phys. **15**, 79 (1978)

28. M. Jayalakshmi, K. Balasubramanian, Int. J. Electrochem. Sci. **3**, 1196 (2008)

29. P. Oruç, S. Eymur, N. Tuğluoğlu, J. Mater. Sci. Mater. Electron. **35**, 314 (2024)

30. A. Teffahi, D. Hamri, A. Djeghlouf, A. Mostefa, M. Arbid, S. Benkraouda, A. Mesli, Phys. B Condens. Matter **701**, 416970 (2025)

31. V.R. Reddy, Thin Solid Films **556**, 300 (2014)

32. İ Dökme, T. Tunç, İ Uslu, Ş Altındal, Synth. Met. **161**, 474 (2011)

33. L.I.N. Zhang, Z.-Y. Cheng, J. Adv. Dielectr. **01**, 389 (2011)

34. A. Ashery, A.E.H. Gaballah, G.M. Turky, M.A. Basyooni-Murat Kabatas, Gels **10**, 537 (2024)

35. H. Praveen, V. Girish Chandran, Polym. Bull. (2025). https://doi.org/10.1007/s00289-025-05724-4

36. S.A. Haladu, K.A. Elsayed, İ Ercan, F. Ercan, T.S. Kayed, T. Demirci, M. Yildiz, S.M. Magami, A.A. Manda, J. Mol. Struct. **1310**, 138262 (2024)

37. H.A.J. Hussien, A. Hashim, J. Inorg. Organomet. Polym. Mater. **34**, 2716 (2024)

38. B. Ghasemi, J. Ševčík, J. Toušková, J. Toušek, P. Klosse, V. Nádaždy, K. Végsö, P. Šiffalovič, B. Hanulíková, M. Urbánek, I. Kuřitka, P. Urbánek, Appl. Surf. Sci. **657**, 159807 (2024)

39. H.M. Alghamdi, A. Rajeh, Sci. Rep. **14**, 18925 (2024)

40. D. Gutiérrez-Armayor, S. Ferrara, M. Nieddu, A. Zieleniewska, R.D. Costa, Adv. Funct. Mater. **35**, 2412921 (2025)

41. M. Yürekli, A.F. Özdemir, Ş Altındal, J. Mater. Sci. Mater. Electron. **35**, 422 (2024)

42. Ö. Sevgili, İ Taşçıoğlu, S. Boughdachi, Y. Azizian-Kalandaragh, Ş Altındal, Phys. B Condens. Matter **566**, 125 (2019)

43. Ş Karataş, J. Mater. Sci. Mater. Electron. **32**, 707 (2021)

44. M. Çavaş, F. Yakuphanoğlu, Ş Karataş, Indian J. Phys. **91**, 413 (2017)

45. Ş Karataş, A. Türüt, Ş Altındal, Radiat. Phys. Chem. **78**, 130 (2009)

46. M. Sebai, A. Hannachi, N. Jaffrezic-Renault, M. Kanzari, Appl. Phys. A **130**, 40 (2023)

47. G. Bousselmi, A. Hannachi, N. Khemiri, M. Kanzari, J. Mater. Sci. Mater. Electron. **35**, 22 (2023)

48. E.H. Nicollian, A. Goetzberger, Bell Syst. Tech. J. **46**, 1055 (1967)

49. A. Kaya, S. Alialy, S. Demirezen, M. Balbaşı, S.A. Yerişkin, A. Aytimur, Ceram. Int. **42**, 3322 (2016)

50. İ Yücedağ, A. Kaya, Ş Altındal, İ Uslu, Chinese Phys. B **23**, 47304 (2014)

51. A. Tataroğlu, Ş Altındal, Microelectron. Eng. **85**, 2256 (2008)

52. I. Hussain, M.Y. Soomro, N. Bano, O. Nur, M. Willander, J. Appl. Phys. **112**, 064506 (2012)

53. Y. Şafak, M. Soylu, F. Yakuphanoğlu, Şemsettin Altındal. J. Appl. Phys. **111**, 034508 (2012)

54. S. Alptekin, Ş Altındal, J. Mater. Sci. Mater. Electron. **31**, 13337 (2020)

55. S. Hameed, Ö. Berkün, S. Altındal Yerişkin, Gazi Univ. J. Sci. Part A Eng. Innov. **11**, 235 (2024)

56. H.G. Çetinkaya, S. Bengi, O. Sevgili, Ş Altındal, Phys. Scr. **99**, 25955 (2024)

57. Ö. Berkün, M. Ulusoy, Ş Altındal, B. Avar, Phys. B Condens. Matter **666**, 415099 (2023)

58. B. Akın, M. Ulusoy, S. Altındal Yerişkin, Mater. Sci. Semicond. Process. **170**, 107951 (2024)

59. N. Urgun, J. Alsmael, S. Altındal Yerişkin, S.O. Tan, Duzce Univ. J. Sci. Technol. **12**, 1964 (2024)

60. C.S. Guclu, Ş Altındal, E. Erbilen Tanrikulu, Phys. B Condens. Matter **677**, 415703 (2024)

61. E. Erbilen Tanrıkulu, İ Taşçıoğlu, J. Electron. Mater. **52**, 2432 (2023)

62. Ç.Ş Güçlü, E.E. Tanrıkulu, M. Ulusoy, Y.A. Kalandargh, Ş Altındal, J. Mater. Sci. Mater. Electron. **35**, 348 (2024)